

Focal deblending

Marine data processing experiences

Kontakis, Apostolos; Verschuur, Dirk Jacob

DOI

[10.1111/1365-2478.13404](https://doi.org/10.1111/1365-2478.13404)

Publication date

2023

Document Version

Final published version

Published in

Geophysical Prospecting

Citation (APA)

Kontakis, A., & Verschuur, D. J. (2023). Focal deblending: Marine data processing experiences. *Geophysical Prospecting*, 72(2), 333-352. <https://doi.org/10.1111/1365-2478.13404>

Important note

To cite this publication, please use the final published version (if applicable).
Please check the document version above.

Copyright

Other than for strictly personal use, it is not permitted to download, forward or distribute the text or part of it, without the consent of the author(s) and/or copyright holder(s), unless the work is under an open content license such as Creative Commons.

Takedown policy

Please contact us and provide details if you believe this document breaches copyrights.
We will remove access to the work immediately and investigate your claim.

Focal deblending: Marine data processing experiences

Apostolos Kontakis  | Dirk Jacob Verschuur

Imaging Physics, Faculty of Applied Sciences, Delft University of Technology, Delft, Zuid Holland, The Netherlands

Correspondence

Apostolos Kontakis, Imaging Physics, Faculty of Applied Sciences, Delft University of Technology, Delft, Zuid Holland, 2628 CD, Netherlands.
Email: a.kontakis@tudelft.nl

Abstract

In contrast to conventional acquisition practices, simultaneous source acquisition allows for overlapping wavefields to be recorded. Relaxing the shot schedule in this manner has certain advantages, such as allowing for faster acquisition and/or denser shot sampling. This flexibility usually comes at the cost of an extra step in the processing workflow, where the wavefields are deblended, that is, separated. An inversion-type algorithm for deblending, based on the focal transform, is investigated. The focal transform uses an approximate velocity model to focus seismic data. The combination of focusing with sparsity constraints is used to suppress blending noise in the deblended wavefield. The focal transform can be defined in different ways to better match the spatial sampling of different types of marine surveys. To avoid solving a large inverse problem, involving a large part of the survey simultaneously, the input data can be split into subsets that are processed independently. We discuss the formation of such sub-sets for ocean bottom node and streamer-type acquisitions. Two deblending experiments are then carried out. The first is on numerically blended ocean bottom node field data. The second is on field-blended towed streamer data with a challenging signal overlap. The latter experiment is repeated using curvelet-based deblending for comparison purposes, showing the virtues of the focal deblending process. Several challenges of basing deblending around the focal transform are discussed as well as some suggestions for improved implementations.

KEYWORDS

data processing, noise, signal processing, seismic acquisition

INTRODUCTION

Nearly simultaneous source acquisition, also referred to as blended acquisition (Berkhout, 2008), differs from conventional acquisition in that seismic wavefields originating from different sources are allowed to overlap in the recorded seismic traces. In conventional acquisition minimal overlap is ensured by requiring that a sufficiently long time interval passes between two consecutive source activations. Blending acquisition relaxes this requirement, allowing more flexibility

in deciding the number of shots, the shot density and the effective acquisition time of a survey (Abma & Foster, 2020; Hampson et al., 2008). By reducing the time required to carry out the acquisition, a blended survey can reduce the amount of recorded noise (Berkhout & Blacqui re, 2013; Moore et al., 2013). Reducing acquisition time can also help schedule the survey such that it is compliant with environmental and other regulations that place limits on survey duration. This can be especially important in marine surveys. If, instead, blended acquisition is used to increase the number

This is an open access article under the terms of the Creative Commons Attribution-NonCommercial-NoDerivs License, which permits use and distribution in any medium, provided the original work is properly cited, the use is non-commercial and no modifications or adaptations are made.

  2023 The Authors. *Geophysical Prospecting* published by John Wiley & Sons Ltd on behalf of European Association of Geoscientists & Engineers.

of source activations, better sub-surface illumination (Abma & Foster, 2020; Berkhout et al., 2010) can be achieved via denser source sampling and having a wider aperture. This can lead to sub-surface illumination with better angle coverage (Blacquière et al., 2012).

The increased shot scheduling flexibility allowed by blended acquisition comes at the cost of having to process blended wavefields. One way of achieving this is by modifying standard processing blocks, such as multiple elimination (Doulgeris, Blacquière, et al., 2012), deghosting (Wu et al., 2016) and migration (Castellanos et al., 2016; Chen et al., 2017; Dai et al., 2011; Li et al., 2016; Tang & Biondi, 2009) to directly handle a blended input. The more popular approach, however, is to apply a wavefield separation/deblending procedure as an independent step, early in the processing workflow. At the acquisition stage, source activation is usually configured to happen in a way that aids the deblending effort. For land acquisition, time and space separation between each overlapping shot can be taken advantage of when deblending. Deblending sometimes further benefits from assigning different sweeps to the seismic sources participating in the acquisition. For marine acquisition, a shot schedule of semi-random inter-shot delays is commonly used (Abma & Foster, 2020). Shot scheduling and characteristics such as sweep profiles define a blending code. The blending code can be used to construct the blending operator, a linear map that maps the desired unblended data to the actually recorded blended data. Deblending methods can be classified depending on how they use this blending operator.

A first approach is to apply the adjoint of the blending operator to the recorded data, followed by a denoising step. Then, the signal to be extracted will become coherent while the blending noise (the interference from other shots) will stay incoherent. The denoising step takes advantage of the incoherence of the blending noise to remove it. Examples of denoising methods used include median filtering (Chen, 2014; Gan et al., 2015; Huo et al., 2012; Y. Liu et al., 2009; Zhang et al., 2013; Z. Liu et al., 2014; Zhan et al., 2015), median filtering after the normal moveout (NMO) correction (Baardman & van Borselen, 2012; Chen et al., 2015), filtering in the wavelet domain (Yu et al., 2017) and using prediction-error filters (Spitz et al., 2008). Recently, deep learning methods have been proposed to tackle the denoising part. Convolutional neural networks (Sun et al., 2020) and U-Nets (Sun et al., 2022) can be trained to map data contaminated with blending noise to clean, denoised data.

The alternative approach is to explicitly have the deblended data honour the blending equation. This is done via a usually iterative, constrained/regularized inversion process. The additional constraints or regularization terms ideally select a solution of the blending equation where blending noise leakage is minimal. For this purpose, Ayeni et al. (2009) use non-stationary dip filters. Doulgeris et al. (2010); Mahdad

et al. (2011); Doulgeris, Mahdad, et al. (2012) use a flexible combination of thresholding and frequency–wavenumber coherency pass filters to progressively estimate and remove blending noise. Zu et al. (2017) use plane wave destruction filtering (Fomel, 2002) in combination with least-squares inversion to achieve separation. Leader and Biondi (2014) extend the imaging condition of reverse time migration (RTM) and use RTM as a deblending tool. Beasley et al. (2016) and Moore et al. (2016, 2017) suggest replacing the inner product operation with a robust version that discriminates against outliers such as impulsive blending noise, guiding the inversion process to a more favourable solution. Transforms that have been used for sparsity-based deblending include Fourier (Abma et al., 2015; Sen et al., 2014), seislets (Chen et al., 2014; Gan et al., 2015), curvelets (Zu et al., 2016), the Radon family (Akerberg et al., 2008; Ayeni et al., 2011; Ibrahim & Sacchi, 2013, 2015; Trad et al., 2012) and multifrequency array steering (Ji et al., 2012). Transform combinations are also possible. Peng and Meng (2016) use both a linear Radon and a wavelet transform in their deblending process. Instead on basing their dictionary on mathematical transforms, Zhou et al. (2013) use dictionary learning to extract it from seismic data. Deep learning solutions can also be used in iterative, inversion-based deblending. Zu et al. (2020) use an iterative inversion similar to that of Mahdad et al. (2011) but with deblended data estimates generated by a combination of convolutional and deconvolutional neural network layers. B. Wang et al. (2022) use iterative inversion and a multi-resolution U-Net to take advantage of the multiscale nature of seismic data. Deep neural network-based approaches can also be used for gradient denoising in iterative schemes, both in a supervised (K. Wang, Mao, et al., 2022; K. Wang & Hu, 2022) and in an unsupervised (K. Wang, Hu, et al., 2022) fashion.

Another way to attack the ill-posed nature of the deblending problem is to assume that the deblended solution will be low rank, that is, few singular values will have significant magnitude when calculating an appropriate singular value decomposition. This can be viewed as an alternative form of sparsity that operates on singular values. This form of sparsity provides us an extra avenue for constraining the deblending problem. An attractive feature of rank reduction methods is that they do not require choosing a dictionary. They do, however, require sorting the elements of the solution into a tensor that exhibits the low-rank property. A popular choice is to form a Hankel matrix out of monochromatic frequency slices of data in the frequency-space domain (Cheng & Sacchi, 2013, 2015; Maraschini et al., 2012). Another approach is to sort the data based on mid-point/half offset coordinates and construct a hierarchically semi-separable matrix from frequency slices (Wason et al., 2014; Kumar et al., 2015). Properly resorted time domain slices are also an option, as demonstrated in Kumar et al. (2016). Since

calculating large singular value decompositions is expensive, computationally cheaper alternatives are sometimes used. For this reason, Cheng and Sacchi (2016) replace singular value decompositions with randomized QR decompositions.

This paper centres around focal deblending, an inversion-type algorithm that is based on the focal transform (Berkhout & Verschuur, 2010; Kutscha & Verschuur, 2012). The focal transform uses an approximate velocity model of the sub-surface and wavefield redatuming to transform a dataset recorded at the surface into a collection of datasets approximately focused at chosen depth levels. The focusing operation allows us to implicitly take advantage of the coherency of the signal to be extracted and, with the help of a sparsity-promoting objective function, discriminate against incoherent blending noise. The focusing process is based on an NMO velocity model. Even though a more detailed interval velocity model – such as one recovered by tomographic methods or full waveform inversion – would be a better choice when it comes to focusing, such models are often not available at the very beginning of the processing chain where deblending will be applied. By picking a few energetic events, an NMO velocity model can also be constructed from moderately blended seismic data.

The first application of focal deblending used the double focal transform (Kontakis & Verschuur, 2014). A combination with the linear Radon transform to better handle events with linear moveout was investigated in Kontakis and Verschuur (2015). When applying an inversion-type deblending process, one of the challenges is to handle the large-scale inversion with vast amounts of data involved. To ease the computational burden, the concept of ‘smart sub-sets’ was introduced later, that is, specially chosen sub-sets of the recorded data, in combination with a suitable definition of the focal transform domain. The concept was first used to process simple synthetic data mimicking a towed streamer acquisition (Kontakis & Verschuur, 2016). In Kontakis et al. (2016), a deblending comparison between the double focal transform (using one-way propagation operators) and the single-sided focal transform (using two-way propagation operators) can be found. The single-sided focal transform was then used in the smart sub-set implementation of focal deblending for ocean bottom node (OBN) surveys (Kontakis & Verschuur, 2017a). A focal-curvelet hybrid approach was investigated in Kontakis and Verschuur (2017b) on synthetic data. In Cao et al. (2019), a greedy matching pursuit solver is compared against spectral projected gradients for the purpose of focal deblending.

In this work, all theory from previous publications, pertaining to marine data processing with focal deblending, is aggregated in one place. The OBN example found in Kontakis and Verschuur (2017a) is revisited, this time using a blending code that leads to a more difficult deblending problem. In addition, a new, challenging towed streamer example is presented. Unlike all previously processed datasets, this one was

blended in the field rather than numerically. The deblending result is then compared with a result produced using sparse curvelet deblending.

This paper is organized as follows. First, the two variants of the focal transform are introduced, as well as the focal deblending optimization problem. The smart sub-set strategy is then described (the Method section). The method is then applied on the two different datasets, each with a separate sub-set configuration (the Examples section). Finally, certain challenges of redatuming-like approaches for deblending are discussed (the Discussion section).

METHOD

The blending equation

For the purposes of this paper, we adopt the convention of representing recorded seismic data as a set of monochromatic frequency slices, following closely the convention introduced in Berkhout (1982). We first consider the case of a non-blended survey. In particular, we assume that the survey is defined by a set \mathcal{S} of n_s unique shot locations and a set \mathcal{R} of n_r unique receiver locations

$$\mathcal{R} = \{\mathbf{x}_1^r, \mathbf{x}_2^r, \dots, \mathbf{x}_{n_r}^r\}, \quad (1)$$

$$\mathcal{S} = \{\mathbf{x}_1^s, \mathbf{x}_2^s, \dots, \mathbf{x}_{n_s}^s\}, \quad (2)$$

where $\mathbf{x}_n^s = (x_n^s, y_n^s, z_n^s)$ and $\mathbf{x}_m^r = (x_m^r, y_m^r, z_m^r)$ are unique source and receiver coordinates, respectively. In a practical acquisition, not all possible combinations of source and receiver locations are realized but rather only a sub-set $\mathcal{A} \subseteq \mathcal{R} \times \mathcal{S}$. In the temporal frequency domain, the pressure samples $p(\mathbf{x}_m^r, \mathbf{x}_n^s; \omega)$ at angular frequency ω can be arranged into a matrix $\mathbf{P}(\omega)$ as follows:

$$[\mathbf{P}(\omega)]_{m,n} = \begin{cases} p(\mathbf{x}_m^r, \mathbf{x}_n^s; \omega) & \text{if } (\mathbf{x}_m^r, \mathbf{x}_n^s) \in \mathcal{A}, \\ 0 & \text{otherwise.} \end{cases} \quad (3)$$

The notation $[\mathbf{P}]_{m,n}$ is used for the (m, n) -th element of matrix \mathbf{P} . Under this arrangement, each column (row) of \mathbf{P} is a frequency slice of a common shot (receiver) gather. Note that in order to keep equations concise, the ω -dependency for matrices will not be marked explicitly, except in definitions and when needed to avoid confusion.

In a blended acquisition, \mathbf{P} is not what is directly recorded but is rather what is ideally recovered by the deblending procedure. Blended data \mathbf{P}_{bl} are recorded instead, the two being related to each other via the blending equation

$$\mathbf{P}_{bl} = \mathbf{P}\mathbf{\Gamma}. \quad (4)$$

We assume here that \mathbf{P}_{bl} is not contaminated by noise generated by sources unrelated to the survey. The blending operator $\mathbf{\Gamma}$ maps unblended to blended data, and for a blending code based on time delays its elements are given by

$$[\mathbf{\Gamma}(\omega)]_{m,n} = \begin{cases} \exp(-j\omega\tau_{m,n}) & \text{if the } m\text{th shot participates in} \\ & \text{the } n\text{th blended shot gather,} \\ 0 & \text{otherwise.} \end{cases} \quad (5)$$

The quantity $\tau_{m,n}$ is the time delay of the source activated at the m th shot location when recording the n th blended shot gather. Unless shot repetition is used (Wu et al., 2015), $\mathbf{\Gamma}$ will have a single nonzero element per row and a total of n_{bl} columns, usually with $n_{\text{bl}} < n_{\text{s}}$. Continuous shooting can be thought of as an extreme case, where there is only one blended gather, that is, $n_{\text{bl}} = 1$ from which all deblended gathers must be extracted.

The adjoint of the blending operator is given by $\mathbf{\Gamma}^{\text{H}}$, with H denoting the complex conjugate transpose of a matrix. Applying it to the blended data produces the pseudo-deblended data \mathbf{P}_{ps}

$$\mathbf{P}_{\text{ps}} = \mathbf{P}_{\text{bl}}\mathbf{\Gamma}^{\text{H}}. \quad (6)$$

Pseudo-deblending for time-delay codes, sometimes referred to as combing (Abma et al., 2015), is the combined action of two operations: (a) copying each blended gather as many times as the number of shots participating in its formation and (b) time shifting each copy in a way that undoes the shift introduced by the time-delay code during acquisition.

The difficulty in extracting \mathbf{P} from \mathbf{P}_{bl} or \mathbf{P}_{ps} stems from the fact that more often than not $\mathbf{\Gamma}$ has non-trivial nullspace. Then, the blending equation (4) on its own does not constrain the problem enough to provide a unique solution for \mathbf{P} . The approach followed here to deal with this problem is to indirectly take advantage of the fact that \mathbf{P} is a wavefield, a significant part of which is generated by scattering in the sub-surface.

The double focal transform

The double focal transform was introduced by Berkhout and Verschuur (2010) and used in Kutscha and Verschuur (2012) for data interpolation. To define the transform, K pairs of depth levels z_k and associated normal moveout (NMO) velocities c_k are chosen. These are usually chosen based on the depths of strong reflectors in the medium. If this information is not available from previous surveys, it can be estimated using semblance analysis on pseudo-deblended data, or picking K strong reflection events and fitting hyperbolae of the form

$$t_{k,m,n} = \sqrt{(t_k^{\text{apex}})^2 + \|\mathbf{x}_m^{\text{r}} - \mathbf{x}_n^{\text{s}}\|^2/c_k^2}, \quad (\mathbf{x}_m^{\text{r}}, \mathbf{x}_n^{\text{s}}) \subseteq \mathcal{A}, \quad (7)$$

$$k = 1, 2, \dots, K$$

to the picks. The hyperbolae are parameterized by t_k^{apex} , the intercept with the time axis at zero offset and the NMO velocity c_k . Each sample $t_{k,m,n}$ is a pick at a trace with receiver coordinates \mathbf{x}_m^{r} , source coordinates \mathbf{x}_n^{s} and is associated with the k th chosen event. The parameters (t_k^{apex}, c_k) can be fitted using least-squares regression on the picks. If a semblance plot is picked instead, the picks will provide the pairs (t_k^{apex}, c_k) directly. Once these parameters are available, the depth levels z_k can be calculated from the pair, using the relationship $z_k = c_k t_k^{\text{apex}}/2$.

For each of these depth levels, a two-dimensional (2D) focal grid of n_q points,

$$\mathcal{Q}^{[k]} = \{\mathbf{q}_1^{[k]}, \mathbf{q}_2^{[k]}, \dots, \mathbf{q}_{n_q}^{[k]}\} \quad (8)$$

is defined, with $\mathbf{q}_m^{[k]} = (x_m^{\text{q}[k]}, y_m^{\text{q}[k]}, z_k)$. The $^{[k]}$ exponent marks the depth level associated with each grid. A strategy for constructing the grid x - and y -coordinates is to define a bounding box around the source–receiver mid-point coordinates and place a rectangular grid over the bounding box. The intersections of the grid lines then define the focal grid points. The x - and y -coordinates can be different per grid, if this is desired.

The purpose of the focal grids is to help represent the dataset recorded at the surface as a superposition of fictitious datasets originating from the K focal grids and redatumed to the surface. These fictitious datasets will be referred to as focal sub-domains. Reconstructing the surface data from the K focal sub-domains \mathbf{X}_k^{D} takes the form

$$\mathbf{P} = \sum_{k=1}^K \mathbf{W}_k^- \mathbf{X}_k^{\text{D}} \mathbf{W}_k^+. \quad (9)$$

The redatuming procedure is carried out with the aid of two one-way extrapolation operators, also referred to here as focal operators. The focal operator \mathbf{W}_k^+ handles downgoing propagation. Its elements are given by

$$[\mathbf{W}_k^+(\omega)]_{(l,n)} = \frac{z_k}{4\pi} \left(\frac{1}{d_{\text{qs}}^3} + \frac{j\omega}{c_k d_{\text{qs}}^2} \right) \exp\left(-\frac{j\omega d_{\text{qs}}}{c_k}\right), \quad (10)$$

$$d_{\text{qs}} = \left\| \mathbf{q}_l^{[k]} - \mathbf{x}_n^{\text{s}} \right\|_2. \quad (11)$$

The elements of \mathbf{W}^+ can be recognized as samples of the vertical derivative of a Green's function from a fictitious source at \mathbf{x}_n^{s} to focal grid point $\mathbf{q}_l^{[k]}$ in a homogeneous medium with

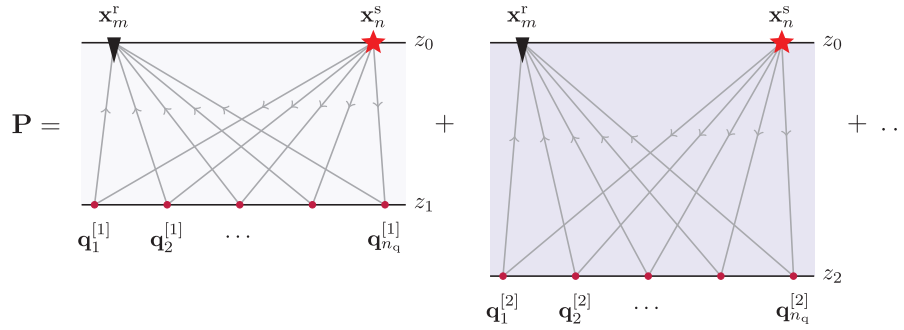


FIGURE 1 Reconstructing a surface trace by redatuming the focal sub-domains at each depth level to the surface. For simplicity, only one lateral dimension is shown.

velocity c_k . Upward propagation is handled by a similarly defined operator

$$[\mathbf{W}_k^-(\omega)]_{(m,l')} = \frac{z_k}{4\pi} \left(\frac{1}{d_{\text{rq}}^3} + \frac{j\omega}{c_k d_{\text{rq}}^2} \right) \exp\left(-\frac{j\omega d_{\text{rq}}}{c_k}\right), \quad (12)$$

$$d_{\text{rq}} = \left\| \mathbf{x}_m^r - \mathbf{q}_{l'}^{[k]} \right\|_2. \quad (13)$$

The difference is that now the focal grid points are linked to the receiver locations. The focal sub-domain \mathbf{X}_k^D is defined as

$$[\mathbf{X}_k^D(\omega)]_{(l',l)} = X_k^D(\mathbf{q}_{l'}^{[k]}, \mathbf{q}_l^{[k]}, \omega), \quad (14)$$

$X_k^D(\mathbf{q}_{l'}^{[k]}, \mathbf{q}_l^{[k]}, \omega)$ being a frequency sample of wavefield generated by a fictitious source at $\mathbf{q}_{l'}^{[k]}$ and recorded by a fictitious receiver placed at $\mathbf{q}_l^{[k]}$. The distance between them is the sub-surface offset. The key property of \mathbf{X}_k^D that will be exploited for deblending is the following. Primary reflections present in \mathbf{P} that are caused by reflectors in the plane $z = z_k$ will be mapped close to the diagonal of \mathbf{X}^D , provided that (a) c_k approximates the true velocity model sufficiently and (b) the focal grid covers the locations where the reflectors are present. This enables some amount of compression, as primary reflections that appear as hyperbolic surfaces in three-dimensional time-domain data can be represented by relatively few elements in \mathbf{X}^D . Yet more informative are time-domain slices $\hat{\mathbf{X}}_k^D(t)$ that can be extracted via the inverse Fourier transform

$$\hat{\mathbf{X}}_k^D(t) = \int_{-\infty}^{+\infty} \mathbf{X}_k^D(\omega) e^{j\omega t} d\omega. \quad (15)$$

In the time domain, primary reflections from the $z = z_k$ plane will map to a band-limited spike centred (time-wise) at the $t = 0$ slice $\hat{\mathbf{X}}_k^D(0)$, if the velocity model is exactly correct and the wavelet was zero-phased. In that case, $\hat{\mathbf{X}}_k^D(0)$ becomes an angle-dependent reflectivity image at depth z_k , which is the link of the focal transform concept with seismic migration (Berkhout and Verschuur, 2010).

In Equation (9), surface data are reconstructed from sub-surface data and can be thought of as a process of defocusing

(see Figure 1). Focusing data into the sub-surface is then the adjoint operation,

$$\mathbf{X}_k^D \approx \mathbf{W}_k^{-H} \mathbf{P} \mathbf{W}_k^{+H}, \quad k = 1, 2, \dots, K. \quad (16)$$

When applied to \mathbf{P} , the complex-conjugate transpose of the focal operators removes traveltime from events and focuses reflections originating from $z = z_k$. An example of the focusing effect can be seen in Figure 2.

The single-sided focal transform

The double focal transform, as presented earlier, uses two one-way operators to handle upgoing and downgoing wavefield extrapolation, from the surface to each chosen depth level. Thus, it requires pre-stack data with proper source and receiver sampling. Another possibility, which we explore here, is to use one two-way operator that extrapolates from the surface to some depth level z_k and back to the surface. This implies that this new extrapolation operator must include scattering in some form, unlike the case of the one-way operators. The concept of using two-way operators is along the thinking found in Berkhout and Verschuur (2006) and can be written as

$$\mathbf{P} = \sum_{k=1}^K \mathbf{W}_k^- \mathbf{I} \mathbf{W}_k^+ \mathbf{X}_k^S = \sum_{k=1}^K \mathbf{W}_k^\pm \mathbf{X}_k^S, \quad (17)$$

where \mathbf{I} is the identity matrix, representing here a locally reacting flat plane reflector at $z = z_k$ with unit reflectivity everywhere. The two-way operator $\mathbf{W}_k^\pm = \mathbf{W}_k^- \mathbf{I} \mathbf{W}_k^+$ models downward propagation through a homogeneous medium, reflection by a fictitious reflector at the plane z_k and upward propagation towards the surface. Each column of the focal sub-domain \mathbf{X}_k^S can be understood as a virtual source array that generates a signal that propagates in the homogeneous medium and generates a component of the corresponding column of \mathbf{P} . Apart from having a separate two-way operator,

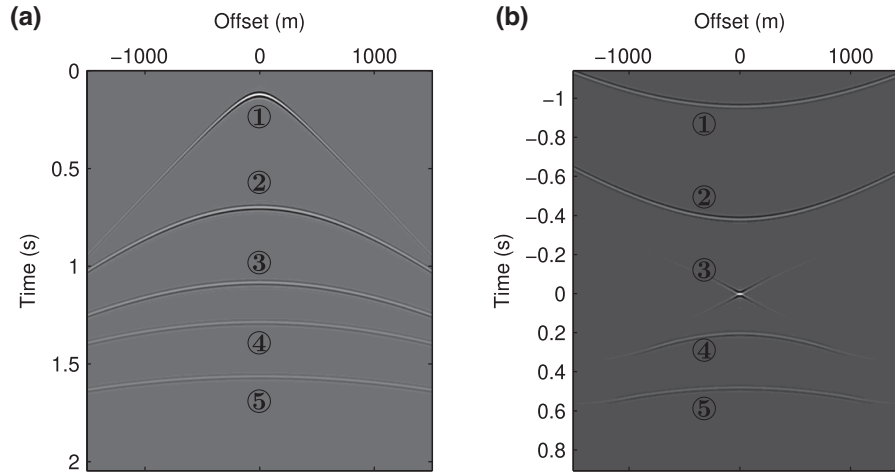


FIGURE 2 (a) One shot gather of an artificial surface dataset with five primary reflection events, in the time domain. (b) The same shot record was extracted from the redatumed dataset and focused at the depth level of the third reflector. The numbers match corresponding events. The third event has been compressed, with most energy concentrated at zero time/sub-surface offset.

each depth level is associated with a different virtual source array. The total \mathbf{P} is given by summing all K components.

One of the main advantages of the single-sided formulation is that this can be applied on a single shot record or common receiver gather, as the focusing happens only on one side of the acquisition grid. However, the focusing properties will depend both on the reflector geometry as well as the velocity accuracy, as in the formulation the reflector geometry is assumed to be flat, represented by the identity matrix. The double-sided focal transform is more versatile, but – as stated earlier – requires good sampling in sources and receivers. Depending on the data acquisition and the chosen sub-set, an optimum choice of focal transform strategy can be made.

Focal deblending

Combining the blending equation (4) with the inverse focal transform (9) yields

$$\mathbf{P}_{\text{bl}} = \sum_{k=1}^K \mathbf{W}_k^- \mathbf{X}_k^D \mathbf{W}_k^+ \mathbf{\Gamma}. \quad (18)$$

Deblending then becomes a problem of solving for the focal sub-domains \mathbf{X}_k^D , rather than for \mathbf{P} directly. The purpose of this detour is to leverage focusing and the sparse representation of seismic events in the focal domain to discriminate against solutions that contain blending noise. The assumption being made here is that solutions $\hat{\mathbf{X}}_{\text{debl},k}^D$ that are free of blending noise are sparser in the space-time domain than those that include it. We promote such sparse solutions by solving the basis pursuit denoising problem (van den Berg & Friedlander,

2008)

$$\left\{ \mathbf{X}_{\text{debl},k}^D(\omega_l) \mid \begin{matrix} l=1,2,\dots,n_f, \\ k=1,2,\dots,K \end{matrix} \right\} = \underset{l=1,2,\dots,n_f, k=1,2,\dots,K}{\text{argmin}} \left\{ \sum_{k=1}^K \sum_{l=1}^{n_f} \left\| \hat{\mathbf{X}}_k^D(t_l) \right\|_S \right\}$$

subject to

$$\sum_{l=1}^{n_f} \left\| \mathbf{P}_{\text{bl}}(\omega_l) - \left(\sum_{k=1}^K \mathbf{W}_k^-(\omega_l) \mathbf{X}_k^D(\omega_l) \mathbf{W}_k^+(\omega_l) \right) \mathbf{\Gamma}(\omega_l) \right\|_F \leq \sigma. \quad (19)$$

Here σ is a parameter that controls the maximum allowed misfit between estimated and observed blended data, n_f is the number of frequency slices and n_t is the number of time slices. The notation

$$\|\mathbf{A}\|_S := \sum_{m,n} |[\mathbf{A}]_{(m,n)}|, \quad \|\mathbf{A}\|_F := \left(\sum_{m,n} |[\mathbf{A}]_{(m,n)}|^2 \right)^{1/2} \quad (20)$$

is used for the sum norm and Frobenius norm of a matrix \mathbf{A} , respectively. The sum norm promotes sparse solutions, which favours preserving the strong components of the focal sub-domains in the deblended result. Ideally, blending noise will not focus equally well due to its incoherent nature and will end up getting suppressed. The optimization takes place over all frequencies and focal sub-domains simultaneously, as one single inversion. The inversion can be handled by iterative solvers, such as SPGL1 (van den Berg & Friedlander, 2008).

The deblended data are then given by applying the inverse focal transform to the deblended focal sub-domains

$$\mathbf{P}_{\text{debl}} = \sum_{k=1}^K \mathbf{W}_k^- \mathbf{X}_{\text{debl},k}^D \mathbf{W}_k^+. \quad (21)$$

Similar expressions can be derived for the single-sided focal transform by replacing $\mathbf{W}_k^- \mathbf{X}_k^D \mathbf{W}_k^+$ with $\mathbf{W}_k^\pm \mathbf{X}_k^S$ in (19) and (21).

Choosing suitable sub-sets

As is most often the case in seismic processing, focusing benefits from having dense source and receiver sampling in all every dimension. In such an ideal scenario, using the entire dataset in the deblending inversion, as is implied in (19), is desirable. It is very rare, however, that each dimension is equally well-sampled in a realistic acquisition. Instead, some dimensions will be coarsely sampled, possibly with very irregular spacing too. As sparsely sampled dimensions will not contribute significantly when focusing, there is motivation to work with well-sampled acquisition sub-sets instead. If the deblending problem could be reduced to a series of smaller, independent, blending problems, this is also beneficial in terms of computational resources needed.

Fortunately, a well-known property of the blending operation can be used to form independent sub-sets of the original data. The property to take advantage of is that each common receiver gather is blended independently. This becomes evident from the blending equation (4). Because of the way the data are organized in \mathbf{P} , each of its rows represents a common receiver gather. The blending operator $\mathbf{\Gamma}$ acts independently per row, deblending each row of \mathbf{P}_{bl} could be treated as a separate deblending problem.

Defining suitable sub-sets will depend on the type of acquisition. For an OBN-type acquisition, receiver sampling is usually sparse and irregular, with source sampling usually much denser. A convenient sub-set then can be formed by considering each node station together with all shots fired while it is recording. For streamer acquisitions, we can make use of the good inline sampling and consider pseudo-2D sub-sets. These are formed by each streamer and the related shots.

Apart from the input data, it is also possible to use the sub-set concept when designing a focal grid. The ideal grid would have dense grid point coverage over the survey area and possibly extend away from it. This however can be rather costly, especially when extensive sub-surface offsets are used. To combat this, the grid can be also chosen based on the data sub-set, by taking advantage of the fact that the most significant amount of scattering recorded by the receivers in the data sub-set will be a localized part of the sub-surface. The optimal choice will depend on the sub-surface structure, but using the mid-point coordinates formed by the sources and the receivers participating in the sub-set is a good starting point. For the OBN and streamer cases examined in this paper, a line was fitted through the mid-points pertaining to a sub-

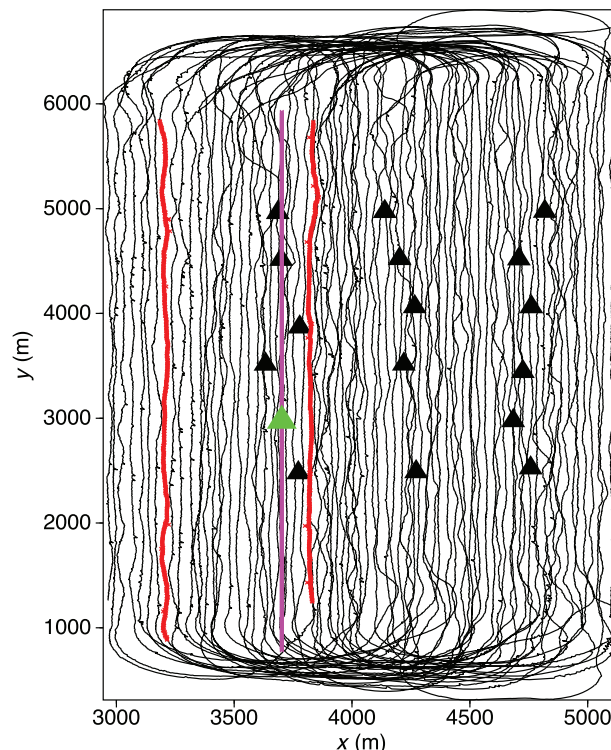


FIGURE 3 Acquisition layout for the OBN example. The black triangles and black lines indicate the nodes and source trajectories, respectively. The extracted shot locations appear in red and the associated receiver node in green. The used focal grid is shown in magenta.

set by linear regression. The focal grid was then constructed either on the line itself or on a narrow strip parallel to the line.

EXAMPLES

Numerically blended ocean bottom node data

The first example also explores focal deblending for ocean bottom node (OBN) data. The data used in the example were acquired by GEOMAR and provided by TEEC. The so-called race-track shooting acquisition layout can be seen in Figure 3. From the total acquisition two shot lines of 700 locations were extracted, the corresponding traces all associated with a particular receiver node. The selected receiver node and shot lines are marked with green and red colour, respectively, in Figure 3. For the OBN case, each common receiver gather naturally forms an independent sub-set. The survey was shot using a dense shot sampling of 6.25 m, on average. Note that in the figures mentioned below, traces have been sub-sampled by a factor of 3 for plotting purposes.

The acquisition was done conventionally, without blending. To create a blended dataset, we assume that there are two

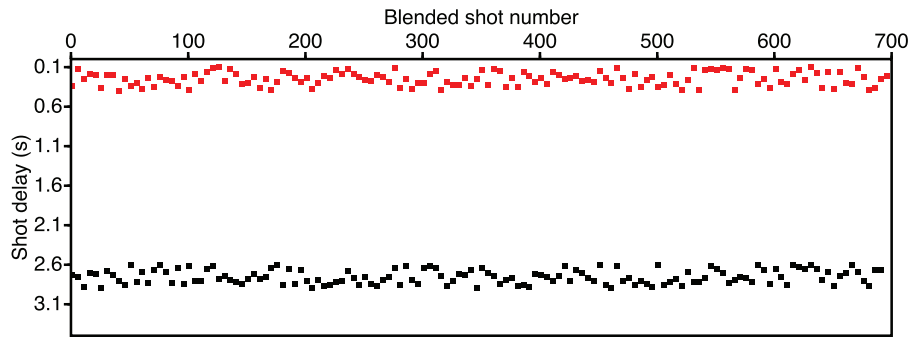


FIGURE 4 The blending code for the OBN example. Each column contains the delay times for a particular blended shot record. Red and black dots represent the first and second shots, respectively.

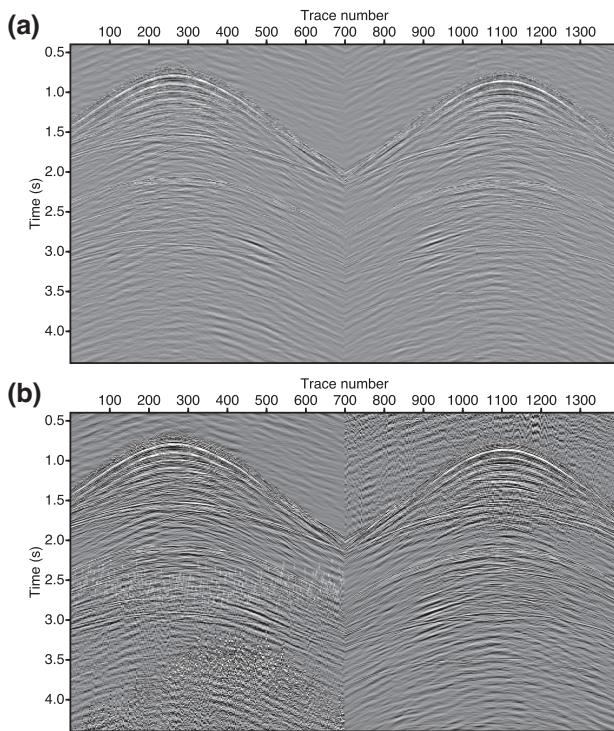


FIGURE 5 OBN example: (a) unblended data and (b) pseudo-deblended data. The visible spatial aliasing effect is only a visual effect as only one out of three traces is plotted.

source vessels, each of which takes care of its own part of the source locations. Each shot was assigned a random time delay code with delays ranging from 0.1 to 0.4 s, with the second sub-set of shots occurring roughly 2.5 s after the first. The delays for each blended shot gather can be seen in Figure 4.

The original, unblended data as well as the data after pseudo-deblending are shown in Figure 5a,b. The time sampling interval was 4 ms, and 3 s of data are kept.

A line along the mid-points defined by the extracted part of the survey acts as a focal grid. In total 735 grid points with a spacing of 7 m are used, for a total of 5138 m. The points are highlighted with a magenta colour in Figure 3.

TABLE 1 Velocities and corresponding zero-offset traveltimes/depths for the focal operators used in the ocean bottom node example.

Operator #	Velocity (m/s)	Traveltime (s)	Depth (m)
1	1482	0.700	519
2	1449	0.740	536
3	1426	0.770	549
4	1593	1.000	797
5	1800	1.540	1386

The grid points in this line define also the sub-surface offset sampling. Since this dataset involves only one receiver, the single-sided focal transform is used for deblending. Five focal sub-domains, defined by the velocities listed in Table 1, were used for focusing/defocusing. Note that the given depth values in Table 1 are only approximations based on the normal moveout (NMO) velocities.

After 600 SPGL1 iterations, the deblended result seen in Figure 6a is obtained. Traces from three out of five focal sub-domains are plotted in Figure 7a–c. The difference from the unblended data in Figure 6b shows some leakage around the sea bottom reflection event; however, most of the blending noise has been effectively suppressed. The remaining blending noise has a laterally inconsistent character, which makes it unlikely to significantly affect migration. As the ground truth, \mathbf{P}_{true} is available for this example; it is possible to assess the deblending quality via the signal-to-blending noise ratio

$$\text{SNR}_{\text{dB}} = 10 \log_{10} \left(\frac{\sum_{\omega} \|\mathbf{P}_{\text{true}}\|_{\text{F}}^2}{\sum_{\omega} \|\mathbf{P}_{\text{debl}} - \mathbf{P}_{\text{true}}\|_{\text{F}}^2} \right). \quad (22)$$

Here, the achieved SNR_{dB} was 26.3 dB.

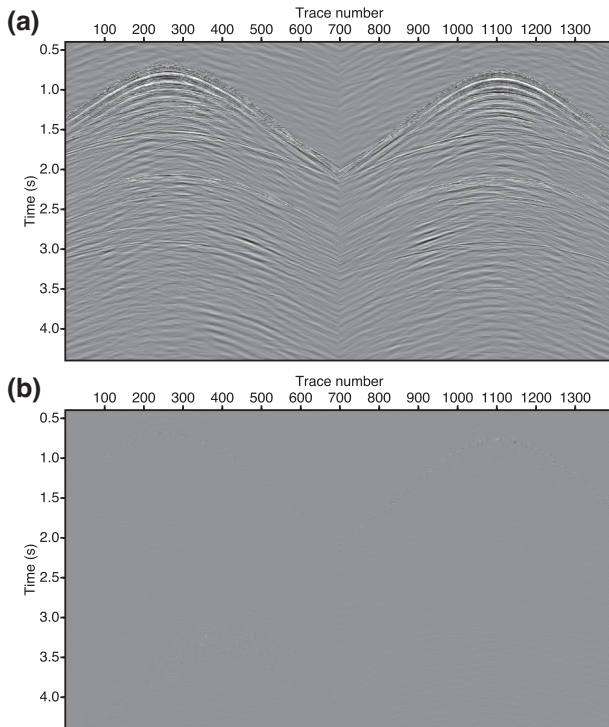


FIGURE 6 OBN example: (a) deblended data and (b) difference between unblended and deblended data, amplified by a factor of 5.

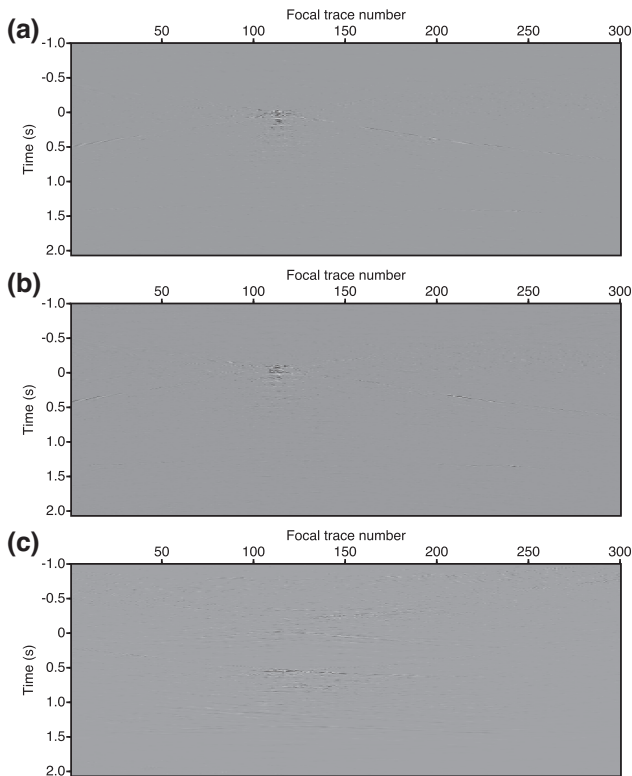


FIGURE 7 OBN example: part of the (a) first, (b) second and (c) fifth focal sub-domain. Similar to the double focal transform, when focusing is achieved most high-amplitude coefficients are concentrated in a small zero time-centred area.

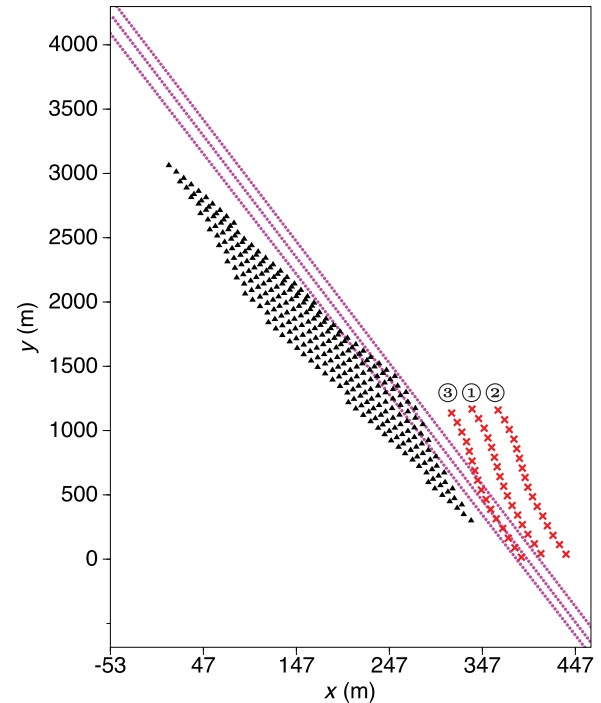


FIGURE 8 Streamer example, selected part of the field-blended acquisition. Red crosses: shot locations; black triangles: receivers on extracted streamer; magenta dots: focal grid points for each airgun sub-set. The numbers indicate the activation pattern used by the three airguns. Note that the x -axis is exaggerated here for plotting purposes.

Field-blended streamer data

The next deblending example is conducted on a sub-set of the Carlsen 3D dataset, provided by TGS. Unlike the previous example, in which numerical blending was used, here the data were blended in the field, as a result of the time interval between subsequent shots. The marine streamer geometry used in the acquisition is depicted in Figure 8. Three airguns were fired sequentially, the first and second activated 33 times and the third 32 times, yielding a total of 98 common shot gathers in the sub-set. The average inline spacing between shots was 37.5 m. The streamer inline spacing for the hydrophones was 12.5 m. Focal deblending was used to deblend up to an offset of 2 km (145 traces per shot), where events exhibit the most curvature and the focal transform is most effective at deblending.

Each shot was fired on average every 5.5 s, with random time dithering in the range of approximately -0.7 to $+0.7$ s. Shot records with a length of 11 s were extracted from the continuous recording. The extraction took place starting from the time instant each source was activated, which then became time zero for the extracted record. This procedure is equivalent to pseudo-deblending as defined in (6), followed by truncation of the pseudo-deblended records at the desired length. The firing times of each shot participating in a

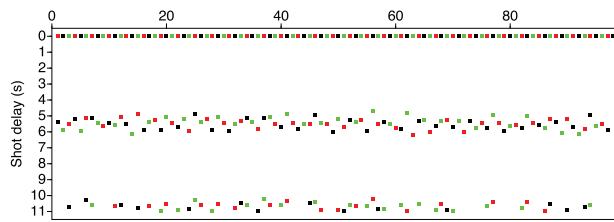


FIGURE 9 The blending code for the field-blended streamer data example. Each column contains the delay times of each shot present in the time window of a particular pseudo-deblended gather. The red, black and green dots correspond to shots by airguns 1, 2 and 3, respectively.

pseudo-deblended shot record can be seen in Figure 9. As the firing times shown are relative, the shot record considered as signal always has a relative time delay of 0 s. The shot records appearing as blending noise have positive delays. In principle, there is also blending noise from previous shots. The assumption made here is that blending noise from previous shots is negligible.

Three different shot gathers before preprocessing are shown in Figure 10, each from a different airgun. The deblending problem is challenging as strong events overlap with weak events of the previous shot. In the first half second, the direct wave and a strong, low-frequency event dominate in amplitude. The latter is probably related to the airgun bubble effect. Such events will not be effectively focused by the focal transform and will tend to dominate the inversion due to their high amplitude. As such, it is better to remove them beforehand to prevent additional blending-noise leakage.

To remove the direct wave and the low-frequency event seen in the near offset, a combination of time windowing and Gabor filtering was used. A time window was constructed based on the time break of the direct wave and the sea-bottom reflection. The common shot gathers pertaining to each airgun were summed, and the result was divided by the number of shot gathers. This stacking process produced an estimate of the direct wave, which mostly stacked constructively within the window. The direct wave estimate was extracted using the previously mentioned time window and was subsequently subtracted from each gather. This action removed most of the direct wave arrival from the shot gathers. The low-frequency event as well as parts of the direct wave still remaining were removed by thresholding in the Gabor time-frequency domain (Spratt, 1988). The data within the time window were transformed to the Gabor domain, where 21% of the highest magnitude components were set to zero. An inverse Gabor transform of the thresholded time-frequency spectrum, followed by time windowing, produced an estimate of the data with the unwanted events removed. This estimate, in combination with the blending code, made it possible to also

subtract these events consistently from all other copies of each common shot gather appearing in the pseudo-deblended data.

To keep the numerical effort and amount of memory required at an affordable level, low-pass filtering up to 45 Hz was performed, followed by subsampling of the dataset from 4 to a 12-ms time sampling interval. The result of this preprocessing can be seen in Figure 11. Comparing with Figure 10, the presence of the direct wave and low-frequency noise is greatly reduced within the first half second. Since this processing was performed per common shot gather with a known blending code, the events removed by processing could also be removed from the blended gather copies such that the processed result was still consistent with the blending equation.

The preprocessed data were given as input for focal deblending. The dataset was divided into three sub-sets, each sub-set containing all shot gathers associated with the same airgun. A focal grid was constructed for each sub-set by sampling a linear segment fitted using the common mid-point coordinates pertaining to each sub-set. The focal grid points were spaced 5 m apart along the linear segment, the total length of which was approximately 5 km. At each grid point, the locations of all other points on the same line within a 500 m radius were used to define local sub-surface offsets. The focal grids used are depicted in Figure 8 as magenta points. The sub-set arrangement used here is ‘pseudo-2D’, in the sense that it consists of a line of shots, a line of receivers and a line grid for the focal, similar to what would happen for a 2D line survey. In reality, the sub-set deviates from being truly 2D due to the presence of some feathering and the fact that the shot and the receiver lines have some distance between them. Placing focal points on a line rather than a grid reduces computational cost but can come at the expense of less focusing for events that originate from the same depth plane but away from the focal grid line.

An independent set of focal sub-domains was used for each sub-set. The associated focal operators used the same velocities/depths for all three sub-sets, but different focal grids for each sub-set. The list of velocities and depths for the eight focal operators is given in Table 2. The moveout for a focal operator may approximately match that of a multiple rather than a primary event. This is in principle not an issue, as long as the focal operator helps reconstruct all events to be part of the deblended data. The double focal transform was used in the inversion problem, and a total of 2000 SPGL1 iterations, taking 16 days for 15 thousand data traces and 4.5 million focal traces on a single 24-core workstation.

The fact that the majority of the events that are responsible for most of the blending noise are in the window from 0 to 5 s is information that can be used to help minimize blending noise leakage in two ways. The first is to use data-domain weighting and give higher weight to residuals of events occurring before 5 s. In this way, they contribute more to the

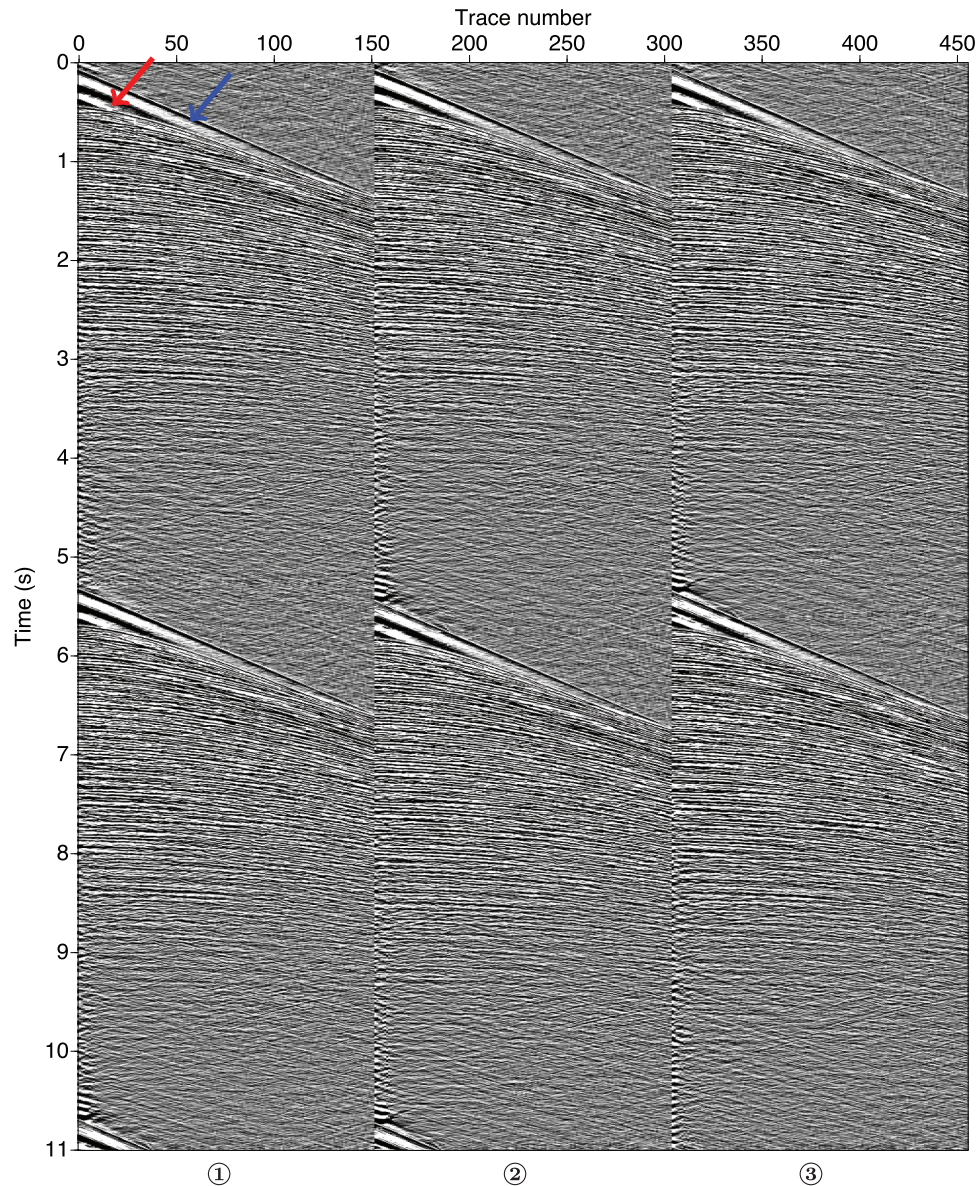


FIGURE 10 Streamer example, pseudo-deblended common shot gathers from the Carlsen 3D dataset, before preprocessing. The number below each gather indicates the airgun number it is associated with. The direct wave and a low-frequency event, likely related to the airgun bubble, are indicated with a blue and red arrow, respectively.

TABLE 2 Velocities and corresponding zero-offset traveltimes/depths for the focal operators used in the streamer example.

Operator #	Velocity (m/s)	Traveltime (s)	Depth (m)
1	1480	0.46	339
2	1572	0.61	483
3	1677	0.76	634
4	1515	1.03	781
5	1499	1.49	1114
6	1589	1.75	1393
7	1577	6.00	4731
8	1670	8.00	6680

ℓ_2 -norm of the residual, making it more likely that they will be explained before the penalized blending noise copies appearing after 5 s. The data-domain weights used here take the form of a sigmoid function having the value 1 before 5 s, transitioning to the value 0.1 after 5 s.

The second possibility, used here in conjunction with the first, is to use focal-domain penalty weights to discourage inclusion of events occurring away from $t = 0$ s in the focal domain, as most signal is expected around the origin while blending noise maps elsewhere. For this particular example, the weight increased linearly in the positive and negative time direction, starting from 1 at 0 s and ending at 10 at ± 5 s. Note that the focal-domain weights are used to implement a

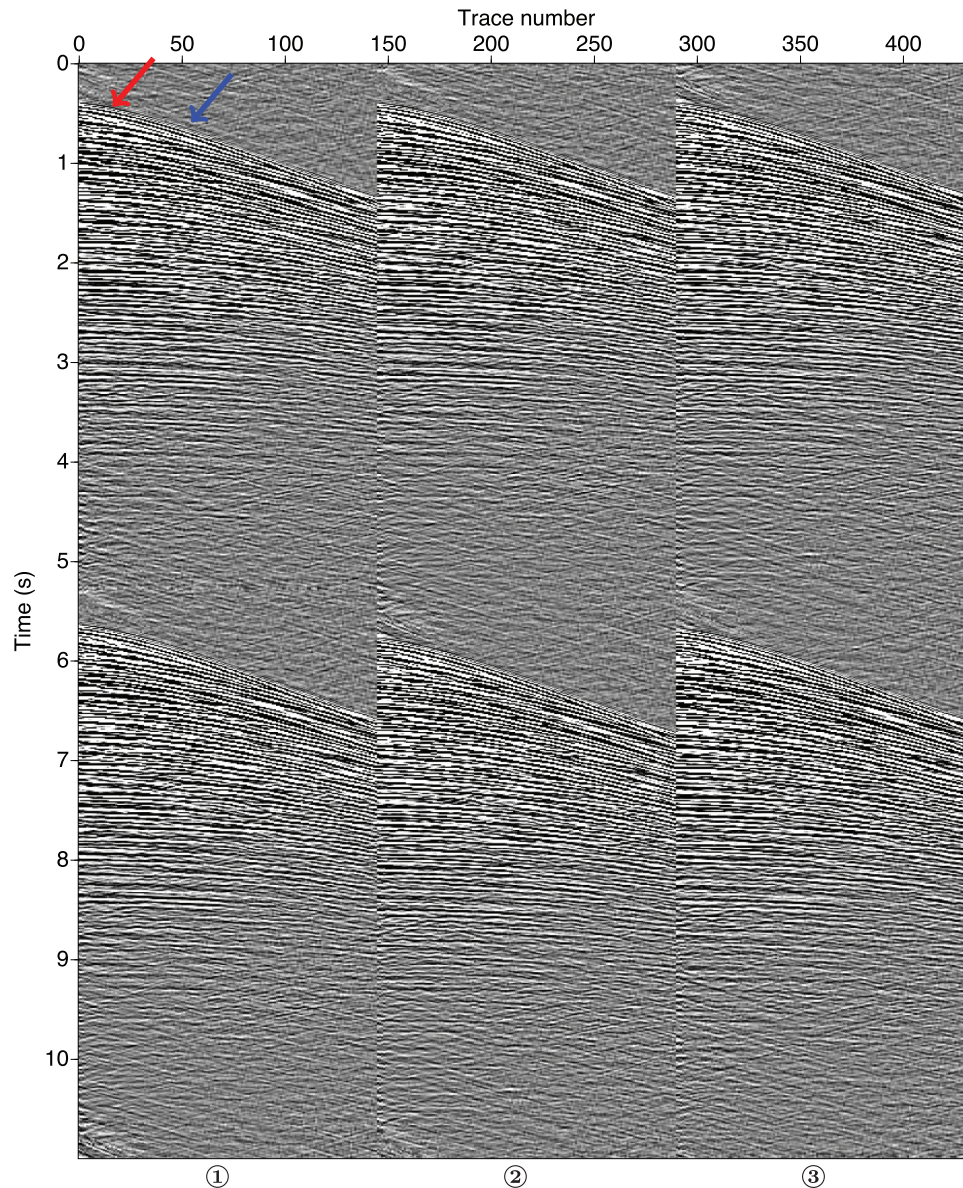


FIGURE 11 Streamer example, pseudo-deblended common shot gathers from the Carlsen 3D dataset, after preprocessing. The number below each gather indicates the airgun number it is associated with. The blue and red arrows indicate the locations of the removed events for the first gather.

weighted ℓ_1 -norm; therefore, unlike in the data-domain case, a higher weight should be interpreted as higher penalty.

As a comparison, the same deblending experiment was repeated using sparse curvelet deblending (Wason et al., 2011; Zu et al., 2018). The streamer receivers were binned according to their x -coordinate, forming bin gathers in which the blending noise was incoherent. The 2D curvelet transform was set up to use four scales and up to 16 wedge angles. Data-domain weights of the same form as the ones used in focal deblending were also applied in the curvelet deblending, except that they transitioned from the value 1 to the value 0.8 after the 5 s mark. A total of 600 SPGL1 iterations were used for curvelet deblending, with a runtime of approximately 3 h.

Three deblended gathers can be seen in Figure 12 for focal deblending and Figure 13 for curvelet deblending. These

correspond to the gathers shown in Figure 11. Despite the challenging blending problem, a lot of the blending noise has been removed by focal deblending, although there is some noticeable blending noise leakage. This is especially evident in the near offset traces. The linear moveout events featured prominently from 5 to 11 s in the deblended result are likely to be a combination of blending noise and transform-related artefacts. Still, a major reduction in blending noise is achieved and original reflection information is recovered that was not visible before. Comparing the deblended gathers from the two methods, it appears that the character of the leaked blending noise is different, with that from focal deblending being lower frequency than that from curvelet deblending.

Because focal sub-domains are not straightforward to interpret, we extract the zero-offset trace for each grid point,

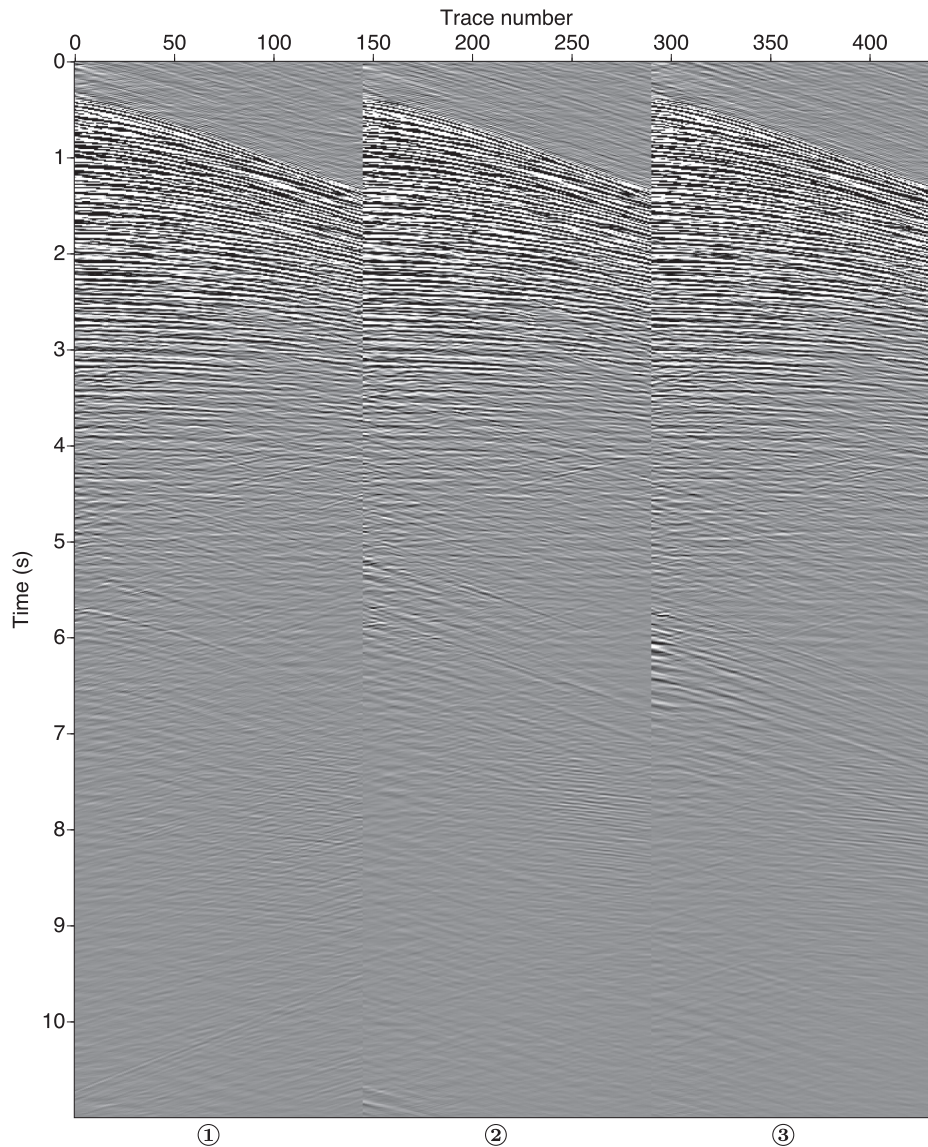


FIGURE 12 Streamer example, debleded common shot gathers using focal deblending. The number below each gather indicates the airgun number it is associated with.

which makes it possible to form image-like gathers, as seen in Figure 14 for four focal sub-domains. These can reveal sub-surface structure and help redesign the focal grid, if needed. The last traces correspond to the grid points furthest from the shot locations. The lower amplitudes seen in this part of the figure hint at lower sub-surface illumination. This is expected, as grid points get further away from source–receiver mid-points. For this particular example, these extra grid points were included to be able to reconstruct weak back-scattered events with opposite dips, present in the large offsets of the input data. From both figures, it can be seen that the focal sub-domains contribute to some extent to events happening away from their target depth.

Events associated with deep reflectors can be very weak to distinguish in pre-stack gathers. In order to assess the recovery of reflector-related information after deblending in the 5 to 11 s time window, stacking was performed after NMO correction

was performed to the data, for both deblending methods. After rotating coordinates such that they are aligned with the y-axis, the dataset was split into common mid-point bins with dimensions $100 \text{ m} \times 12.5 \text{ m}$. The NMO-corrected traces within each bin were then to produce a stack gather.

For comparison purposes, the same stacking procedure was repeated with the pseudo-debleded input data. The stacked input and stacked debleded output for focal and curvelet deblending are shown in Figure 15a–c, respectively. A linear time gain was applied to amplify the deeper events. In both cases, some blending noise leakage is clearly visible even after deblending and is associated with the near-offset blending noise seen relatively consistently in most debleded gathers. Due to the low number of shots, the stacking power is not enough to reveal weak events in the areas marked by red arrows. In the mid-offsets, however, certain reflectors that were completely masked by blending noise input become

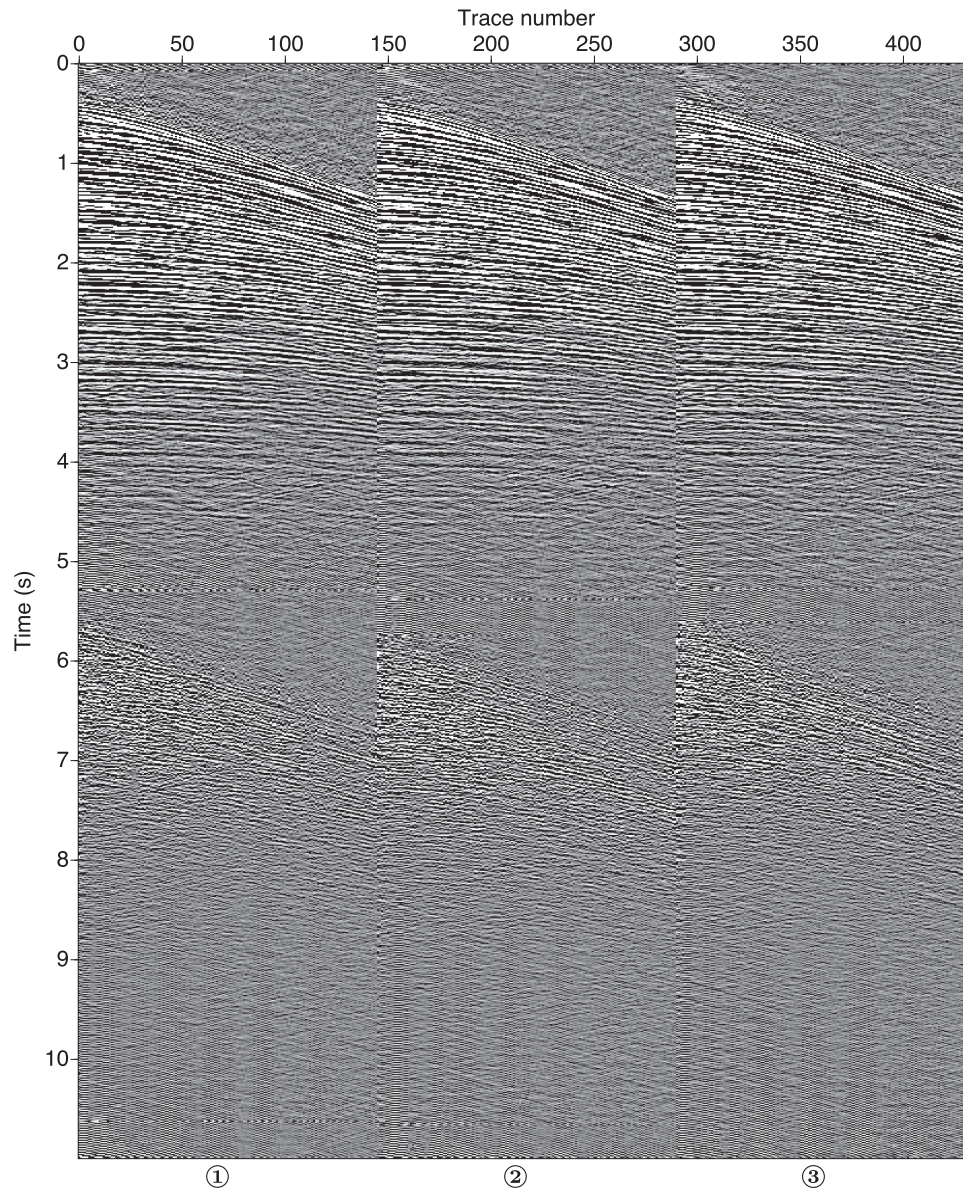


FIGURE 13 Streamer example, debled common shot gathers using curvelet debrending. The number below each gather indicates the airgun number it is associated with.

discernible. These are indicated with green arrows in Figure, 15b,d, showing the possibility to recover some sub-surface information generating weak events even after the 5-s mark. This can be seen more clearly in Figure 15c,e, where linear Radon and curvelet filtering has been applied to attenuate blending noise leakage and transform artefacts. Note that the better separation achieved by focal debrending has produced reflectors that are more clearly visible in the middle part of the stack sections.

DISCUSSION

Accuracy of the velocity model

The choice to use picked normal moveout (NMO) velocities for defining the focal operators makes their implementation

relatively simple and straightforward. It also makes the method more suitable for application on data acquired in new areas, for which pre-existing sub-surface models do not yet exist. Assuming a moderate amount of blending noise, the NMO velocities can be picked directly from pseudo-debled data. Relying on a simple velocity model, however, comes at a cost. An obvious one is imperfect focusing, as errors in the velocity model translate to errors in calculated traveltimes from the sub-surface focal grid points to the sources and receivers at the surface level. Erroneous traveltimes will compromise focusing power to some extent, due to sub-optimal trace stacking. This, in turn, may make sparsity promotion less effective as a strategy for suppressing blending noise leakage.

A possible remedy would be to move towards a more accurate velocity model and use more finely spaced depth levels,

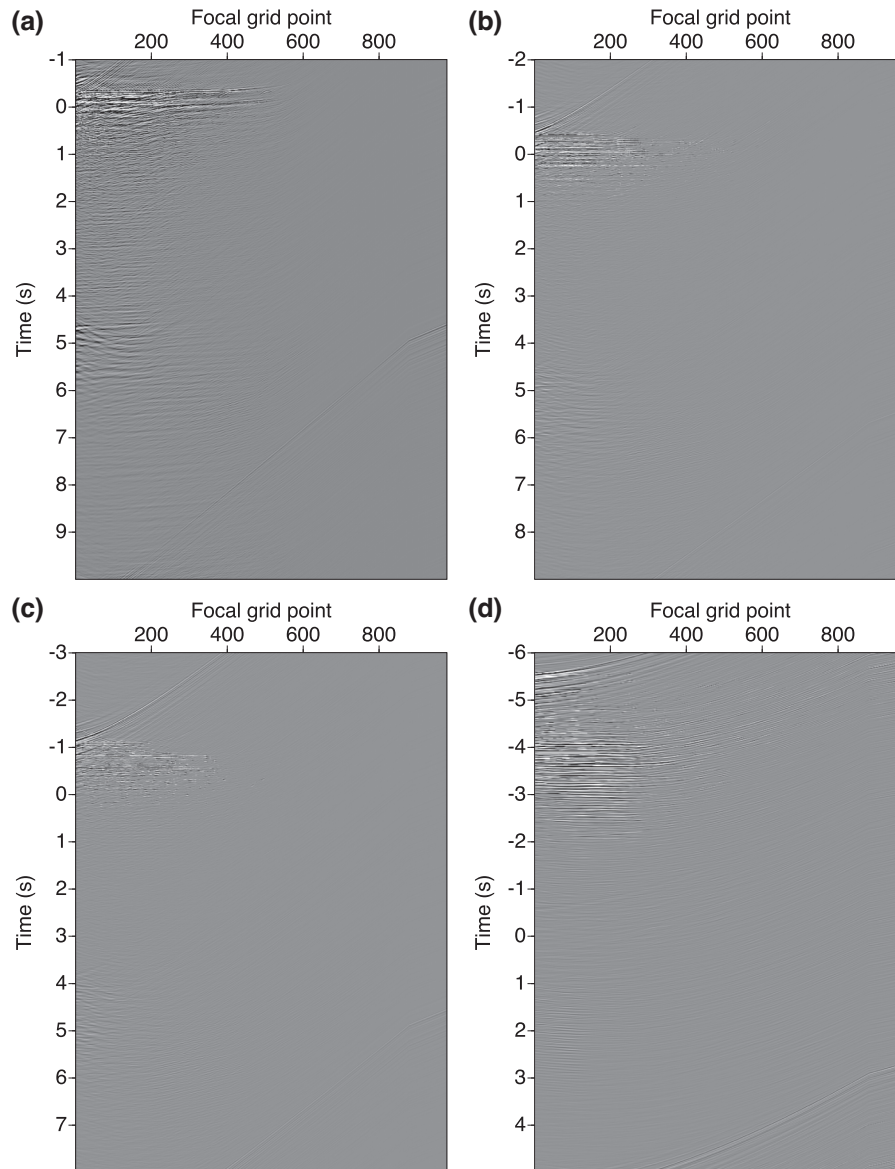


FIGURE 14 Streamer example, focal sub-domain zero local offset gather for the first airgun sub-set: (a) first sub-domain, (b) third sub-domain, (c) fifth sub-domain and (d) seventh sub-domain. Note the different time axes for each plot.

that is, move closer to migration. The focal sub-domains then could be made to have a shorter time extent and their content would approximate more closely interface reflectivity at particular depth levels. A more sophisticated modelling engine, such as joint migration inversion could be then used to not only produce primary events from the focal sub-domains but also the associated multiples as well as a suitable velocity model (Berkhout, 2014). This leads to a more compressed representation of the surface data, as multiples would not need to be represented as fictitious primary events, as is currently the case. Accurate velocities would be important for this, as inaccuracies would produce multiples that do not match in time those present in the recorded data, especially when modelling higher orders of multiples.

Range of the focal operators

As currently implemented, the focal transform is based on constant-velocity wavefield propagators. In the frequency-wavenumber (FK) domain they take the form $\exp(j(\omega^2/c^2 - k_x^2 - k_y^2)^{1/2}z)$. For $(k_x^2 + k_y^2)^{1/2} > |\omega/c|$, the propagator is in the evanescent region, exponentially decaying in amplitude. Due to limited floating point precision, the operator essentially takes the value zero for high wavenumbers, which creates an effective nullspace. In other words, the operator functions as an FK filter, and the associated focal sub-domain cannot fully represent events which have a spectral content that exceeds ω/c in the FK domain.

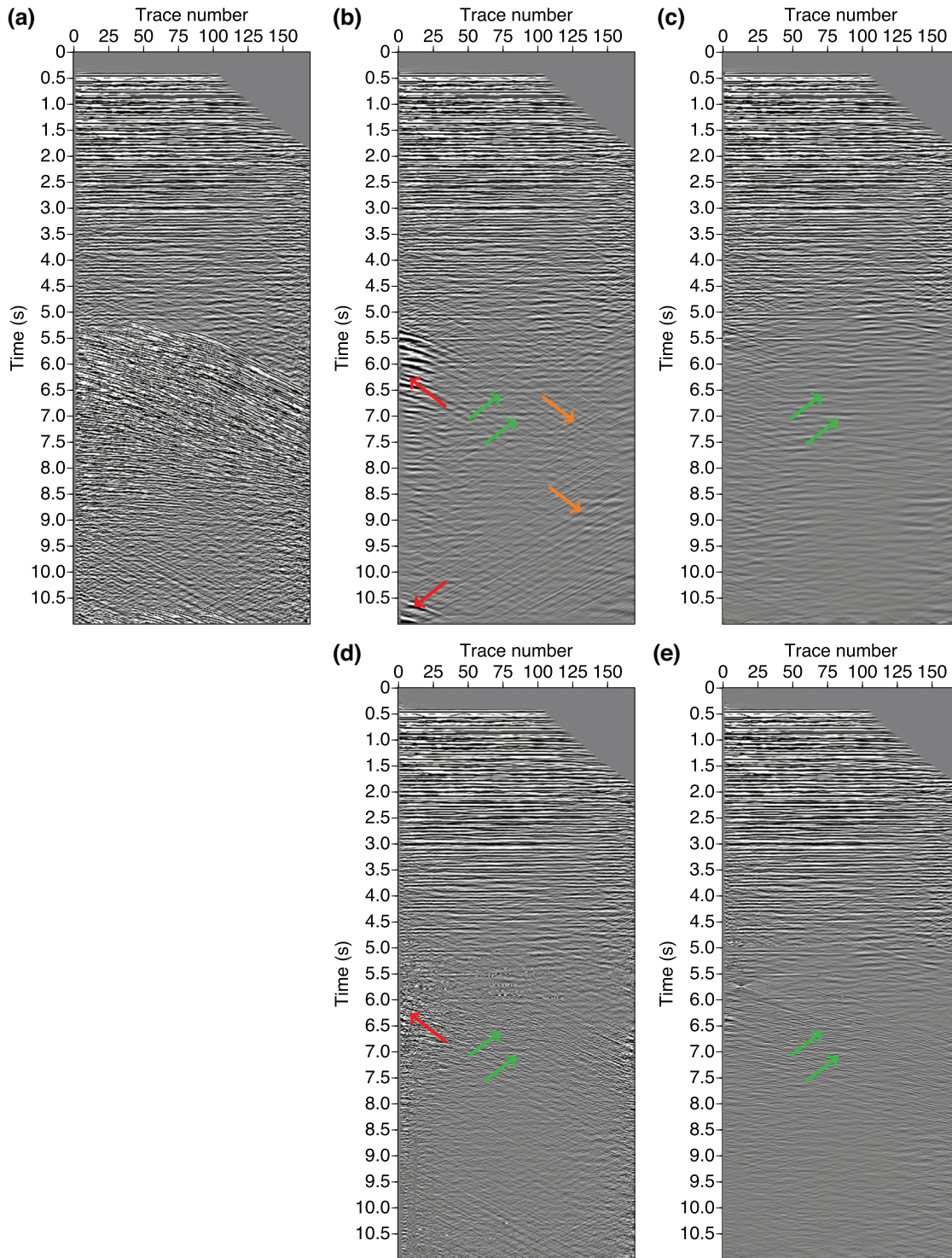


FIGURE 15 Streamer example, stacked data: (a) before deblending, (b) after focal deblending, (c) after filtering the focal deblending stack, (d) after curvelet deblending and (e) after filtering the curvelet deblending stack. A combination of linear Radon and curvelet filtering was used in both cases to remove noise leakage at the edges and transform artefacts. Red arrows indicate areas of excessive blending noise leakage. Green arrows indicate recovered reflectors. Orange arrows point at what are likely transform artefacts.

This is a double-edged sword when it comes to deblending. The positive aspect is that part of the blending noise will be filtered out too. This is a consequence of the random time delay code, which makes blending noise in common receiver gathers incoherent and broad-spectrum. The negative aspect is that part of the signal may not be recoverable. Worse, if the blending noise associated with that part of the signal is mapped to wavenumbers below $|\omega/c|$, then it may enter the solution as (and only as) blending noise.

This issue is not limited to the focal transform but may occur whenever the ground-truth deblended data cannot be represented as a linear combination of the atoms of the chosen dictionary, for example, when a linear Radon transform with insufficient coverage of ray parameters is used. For the case of the focal transform, the problem can be partially remedied by making sure that one of the focal operators is chosen with a velocity c that accommodates for the events in the data with the slowest moveout.

Shape of the focal transform atoms

In the time-space domain, each atom of the dictionary defined by the focal transform has a hyperbolic moveout. This makes the focal transform good at capturing the curved near-offset part of events as well as diffractions. It struggles, however, to explain very local features, such as sudden changes in amplitude. These can be caused by anomalies in the gain settings of hydrophones or differences in airgun strength between shots. These issues would need to be resolved before deblending, as a separate step. This is probably true for most transform-based deblending algorithms. The atoms themselves in principle extend spatially to infinity, but geometric spreading somewhat limits in practice this extent, making the atom more localized. Still, very local features can be difficult to explain as the composition of few atoms. This is an area where having a concept of scale, such as that shared by the wavelet and curvelet family of transforms, can be beneficial (Kontakis & Verschuur, 2017b).

It should be noted, however, that the capability of explaining very local features also has a disadvantage when time delay codes are used for blending. The problem is that occasionally blending noise will itself manifest as local feature, for example, as an amplitude spike surrounded by lower amplitude events. If such a feature can be sparsely explained by a few atoms in the dictionary then that makes it more likely that noise will find its way into the solution when sparsity constraints are used.

Computational cost

Another important criterion for assessing seismic processing tools is their computational cost. We assume for simplic-

ity that the survey has an approximately equal $n_r = n_s = n$ unique source/receiver coordinate and that the focal grid is also defined by n points. Then, each focusing/defocusing step requires approximately $2Kn_f n^3$ complex multiplications, needed to carry out the two matrix–matrix multiplications in (9), n_f being the number of frequency slices and K the number of focal sub-domains. The focusing and defocusing operations may need to be performed multiple times per each of the several hundreds of iterations. The number of arithmetic operations roughly scales with the third power in terms of survey size. This estimate is rather pessimistic, as usually the source and receiver dimensions are rarely equally well-sampled in practice. The computational cost is still rather steep.

A way to remedy this is to work with sub-sets of the data, as was done for the examples discussed in this paper. This does not change the scaling properties of the problem but reduces n , which can have a significant impact on execution time. A way to improve the scaling with respect to survey size is to use fast multipole methods (FMM) (Cheng et al., 2006) to carry out matrix multiplications involving \mathbf{W}_k^- and \mathbf{W}_k^+ . The FMM reduces the numerical effort required for matrix–vector multiplications by exploiting the low-rank properties of matrices constructed as in (10) and (12). The main challenge with the FMM is the rather sophisticated implementation that is required, compared to the straightforward approach of implementing (9) as described in the Method section.

CONCLUSIONS

A deblending method based on seismic data focusing was presented. By using a focal operator based on a velocity model, prior knowledge can be included to enhance focusing, while a sparse inversion engine ensures that the unblended data can be effectively described. Instead of solving one large inverse problem, a proposal for using smart sub-sets of the seismic data and of the focal domain was made, depending on the acquisition layout. The field data examples on ocean bottom node and streamer acquisitions indicate that the focal transform can help remove a significant amount of blending noise. Due to the need for sub-surface offsets and full redatuming-like steps, however, the computational cost can be considerable. Using the focusing properties of the seismic wavefields is an interesting alternative approach to wavefield separation, which is especially beneficial for the curved parts of the wavefields.

ACKNOWLEDGEMENTS


The authors would like to thank TEEC and GEOMAR for providing the field data used in the OBN example, TGS for providing the field data used in the streamer example as well as the authors of the SPGL1 solver (van den Berg & Friedlander, 2007). The views and opinions expressed in this work

are those of the authors and not necessarily shared by GEOMAR, TEEC and TGS. The authors would also like to thank the sponsors of the Delphi consortium for their support.

DATA AVAILABILITY STATEMENT

The data that support the findings will not be available.

ORCID

Apostolos Kontakis  <https://orcid.org/0000-0003-3634-1010>

REFERENCES

- Abma, R. & Foster, M.S. (2020) *Simultaneous source seismic acquisition*. Houston, TX: Society of Exploration Geophysicists.
- Abma, R., Howe, D., Foster, M., Ahmed, I., Tanis, M., Zhang, Q., Arogunmati, A. & Alexander, G. (2015) Independent simultaneous source acquisition and processing. *Geophysics*, 80, WD37–WD44.
- Akerberg, P., Hampson, G., Rickett, J., Martin, H. & Cole, J. (2008) Simultaneous source separation by sparse Radon transform. In *78th SEG Annual International Meeting, Expanded Abstracts*. Houston, TX: Society of Exploration Geophysicists, pp. 2801–2805.
- Ayeni, G., Almomin, A. & Nichols, D. (2011) On the separation of simultaneous–source data by inversion. In *81st SEG Annual International Meeting, Expanded Abstracts*. Houston, TX: Society of Exploration Geophysicists, pages 20–25.
- Ayeni, G., Tang, Y. & Biondi, B. (2009) Joint preconditioned least-squares inversion of simultaneous source time–lapse seismic data sets. In *79th SEG Annual International Meeting, Expanded Abstracts*. Houston, TX: Society of Exploration Geophysicists, pp. 3914–3918.
- Baardman, R. & van Borselen, R. (2012) Separating sources in marine simultaneous shooting acquisition – method & applications. In *82nd SEG Annual International Meeting, Expanded Abstracts*. Houston, TX: Society of Exploration Geophysicists, pp. 1–5.
- Beasley, C., Moore, I., Fletcher, R. & Castellanos, C. (2016) Simultaneous source separation using adaptive robust linear algebra. In *78th EAGE Conference & Exhibition, Extended Abstracts*. Houten, the Netherlands: European Association of Geoscientists & Engineers, p. We LHR2 07.
- Berkhout, A.J. (2014) An outlook on the future of seismic imaging, part iii: joint migration inversion. *Geophysical Prospecting*, 62, 950–971.
- Berkhout, A.J. (1982) *Seismic migration, imaging of acoustic energy by wave field extrapolation, A: Theoretical aspects*, 2nd edition. Amsterdam: Elsevier.
- Berkhout, A.J. (2008) Changing the mindset in seismic data acquisition. *The Leading Edge*, 27, 924–938.
- Berkhout, A.J. & Blacquièrre, G. (2013) Effect of noise in blending and deblending. In *83rd SEG Annual International Meeting, Expanded Abstracts*. Houston, TX: Society of Exploration Geophysicists, pp. 94–98.
- Berkhout, A.J., Blacquièrre, G. & Verschuur, D.J. (2010) Multi-scattering illumination in blended acquisition design. In *80th SEG Annual International Meeting, Expanded Abstracts*. Houston, TX: Society of Exploration Geophysicists, pp. 1251–1255.
- Berkhout, A.J. & Verschuur, D.J. (2006) Focal transformation, an imaging concept for signal restoration and noise removal. *Geophysics*, 71, A55–A59.
- Berkhout, A.J. & Verschuur, D.J. (2010) Parameterization of seismic data using gridpoint responses. In *80th SEG Annual International Meeting, Expanded Abstracts*. Houston, TX: Society of Exploration Geophysicists, pp. 3344–3348.
- Blacquièrre, G., Berkhout, A.J. & Verschuur, D.J. (2012) Double illumination in blended acquisition. In *82nd SEG Annual International Meeting, Expanded Abstracts*. Houston, TX: Society of Exploration Geophysicists, pp. 11–15.
- Cao, J., Kontakis, A., Verschuur, D.J., Gu, H. & Li, L. (2019) Deblending using the focal transformation with an efficient greedy inversion solver. *Journal of Applied Geophysics*, 170, 103–109.
- Castellanos, C., Fletcher, R., Moore, I. & Beasley, C. (2016) Removing simultaneous source crosstalk with reverse time migration. In *86th SEG Annual International Meeting, Expanded Abstracts*. Houston, TX: Society of Exploration Geophysicists, pp. 4305–4309.
- Chen, Y. (2014) Deblending using a space-varying median filter. In *84th SEG Annual International Meeting, Expanded Abstracts*. Houston, TX: Society of Exploration Geophysicists, pp. 82–87.
- Chen, Y., Chen, H., Xiang, K. & Chen, X. (2017) Preserving the discontinuities in least-squares reverse time migration of simultaneous-source data. *Geophysics*, 82, S185–S196.
- Chen, Y., Fomel, S. & Hu, J. (2014) Iterative deblending of simultaneous-source seismic data using seislet-domain shaping regularization. *Geophysics*, 79, V179–V189.
- Chen, Y., Jin, Z., Gan, S., Yang, W. & Xiang, K. (2015) Deblending using a combined PNMO-MF-FK coherency filter. In *85th SEG Annual International Meeting, Expanded Abstracts*. Houston, TX: Society of Exploration Geophysicists, pp. 3920–3925.
- Cheng, H., Crutchfield, W.Y., Gimbutas, Z., Greengard, L.F., Ethridge, J.F., Huang, J., Rokhlin, V., Yarvin, N. & Zhao, J. (2006) A wideband fast multipole method for the Helmholtz equation in three dimensions. *Journal of Computational Physics*, 216, 300–325.
- Cheng, J. & Sacchi, M.D. (2013) Separation of simultaneous source data via iterative rank reduction. In *83rd SEG Annual International Meeting, Expanded Abstracts*. Houston, TX: Society of Exploration Geophysicists, pp. 88–93.
- Cheng, J. & Sacchi, M.D. (2015) Separation and reconstruction of simultaneous source data via iterative rank reduction. *Geophysics*, 80, V57–V66.
- Cheng, J. & Sacchi, M.D. (2016) Fast dual-domain reduced-rank algorithm for 3D deblending via randomized QR decomposition. *Geophysics*, 81, V89–V101.
- Dai, W., Wang, X. & Schuster, G.T. (2011) Least-squares migration of multisource data with a deblurring filter. *Geophysics*, 76, R135–R146.
- Dougeris, P., Blacquièrre, G. & Verschuur, E. (2012) Integration of deblending and surface-related multiple elimination: application to marine data. In *82nd SEG Annual International Meeting, Expanded Abstracts*. Houston, TX: Society of Exploration Geophysicists, pp. 1–6.
- Dougeris, P., Mahdad, A. & Blacquièrre, G. (2010) Separation of blended data by iterative estimation and subtraction of interference noise. In *80th SEG Annual International Meeting, Expanded Abstracts*. Houston, TX: Society of Exploration Geophysicists, pp. 3514–3518.
- Dougeris, P., Mahdad, A. & Blacquièrre, G. (2012) Iterative separation of blended marine data: discussion on the coherence–pass filter. In *82nd*

- SEG Annual International Meeting, Expanded Abstracts. Houston, TX: Society of Exploration Geophysicists, pp. 26–31.
- Fomel, S. (2002) Applications of plane-wave destruction filters. *Geophysics*, 67, 1946–1960.
- Gan, S., Wang, S., Chen, X. & Chen, Y. (2015) Deblending using a structural-oriented median filter. In *85th SEG Annual International Meeting, Expanded Abstracts*. Houston, TX: Society of Exploration Geophysicists, pp. 59–64.
- Hampson, G., Stefani, J. & Herkenhoff, F. (2008) Acquisition using simultaneous sources. In *78th SEG Annual International Meeting, Expanded Abstracts*. Houston, TX: Society of Exploration Geophysicists, pp. 2816–2820.
- Huo, S., Luo, Y. & Kelamis, P.G. (2012) Simultaneous sources separation via multidirectional vector-median filtering. *Geophysics*, 77, V123–V131.
- Ibrahim, A. & Sacchi, M.D. (2013) Simultaneous source separation using a robust Radon transform. *Geophysics*, 79, V1–V11.
- Ibrahim, A. & Sacchi, M.D. (2015) Fast simultaneous seismic source separation using Stolt migration and demigration operators. *Geophysics*, 80, WD27–WD36.
- Ji, Y., Kragh, E. & Christie, P. (2012) A new simultaneous source separation algorithm using frequency-diverse filtering. In *82nd SEG Annual International Meeting, Expanded Abstracts*. Houston, TX: Society of Exploration Geophysicists, pp. 1–5.
- Kontakis, A. & Verschuur, D.J. (2014) Deblending via sparsity-constrained inversion in the focal domain. In *76th EAGE Conference & Exhibition, Extended Abstracts*. Houten, the Netherlands: European Association of Geoscientists & Engineers., p. Th ELI2 02.
- Kontakis, A. & Verschuur, D.J. (2015) Deblending via a hybrid focal and linear radon transform. In *77th EAGE Conference & Exhibition, Extended Abstracts*. Houten, the Netherlands: European Association of Geoscientists & Engineers, pp. We N101 02.
- Kontakis, A. & Verschuur, D.J. (2016) Focal deblending using smart subsets of towed streamer 5d data. In *86th SEG Annual International Meeting, Expanded Abstracts*. Houston, TX: Society of Exploration Geophysicists, pp. 4612–4617.
- Kontakis, A. & Verschuur, D.J. (2017a) Focal deblending using smart subsets of OBN 5D data. In *79th EAGE Conference & Exhibition, Extended Abstracts*. Houten, the Netherlands: European Association of Geoscientists & Engineers, p. We P3 11.
- Kontakis, A. & Verschuur, D.J. (2017b) Using a hybrid focal – curvelet transform for deblending. In *87th SEG Annual International Meeting, Expanded Abstracts*. Houston, TX: Society of Exploration Geophysicists, pp. 4903–4908.
- Kontakis, A., Wu, S. & Verschuur, D.J. (2016) Acquisition geometry-aware focal deblending. In *78th EAGE Conference & Exhibition, Extended Abstracts*. Houten, the Netherlands: European Association of Geoscientists & Engineers, p. Th P4 05.
- Kumar, R., Sharan, S., Wason, H. & Herrmann, F. (2016) Time-jittered marine acquisition: A rank-minimization approach for 5D source separation. In *SEG Technical Program Expanded Abstracts Expanded Abstracts 2016*. Houston, TX: Society of Exploration Geophysicists, pp. 119–123.
- Kumar, R., Wason, H. & Herrmann, F.J. (2015) Source separation for simultaneous towed-streamer marine acquisition – A compressed sensing approach. *Geophysics*, 80, WD73–WD88.
- Kutscha, H. & Verschuur, D.J. (2012) Data reconstruction via sparse double focal transformation: An overview. *Signal Processing Magazine, IEEE*, 29, 53–60.
- Leader, C. & Biondi, B. (2014) Demigration and image space separation of simultaneously acquired data. In *84th SEG Annual International Meeting, Expanded Abstracts*. Houston, TX: Society of Exploration Geophysicists, pp. 88–93.
- Li, C., Huang, J. & Li, Z. (2016) Regularized least-squares reverse time migration of simultaneous-source data with adaptive singular spectrum analysis. In *86th SEG Annual International Meeting, Expanded Abstracts*. Houston, TX: Society of Exploration Geophysicists, pp. 4419–4423.
- Liu, Y., Luo, Y. & Wang, Y. (2009) Vector median filter and its applications in geophysics. In *79th SEG Annual International Meeting, Expanded Abstracts*. Houston, TX: Society of Exploration Geophysicists, pp. 3342–3346.
- Liu, Z., Wang, B., Specht, J., Sposato, J. & Zhai, Y. (2014) Enhanced adaptive subtraction method for simultaneous source separation. In *84th SEG Annual International Meeting, Expanded Abstracts*. Houston, TX: Society of Exploration Geophysicists, pp. 115–119.
- Mahdad, A., Doulgeris, P. & Blacquièrre, G. (2011) Separation of blended data by iterative estimation and subtraction of blending interference noise. *Geophysics*, 76, Q9–Q17.
- Maraschini, M., Dyer, R., Stevens, K., Bird, D. & King, S. (2012) An iterative SVD method for deblending: theory and examples. In *82nd SEG Annual International Meeting, Expanded Abstracts*. Houston, TX: Society of Exploration Geophysicists, pp. 1–5.
- Moore, I., Beasley, C. & Fletcher, R. (2017) The roles of sparseness and robust linear algebra in simultaneous-source separation. In *79th EAGE Conference & Exhibition, Extended Abstracts*. Houten, the Netherlands: European Association of Geoscientists & Engineers, p. We P3 10.
- Moore, I., Bisley, R., Beasley, C., Bayly, M., Monk, D. & Hansen, L. (2013) Simultaneous-source acquisition and environmental noise – good or bad? In *75th EAGE Conference & Exhibition, Extended Abstracts*. Houten, the Netherlands: European Association of Geoscientists & Engineers, p. Th 08 03.
- Moore, I., Fletcher, R., Beasley, C. & Castellanos, C. (2016) Data studies of simultaneous source separation using robust linear algebra. In *86th SEG Annual International Meeting, Expanded Abstracts*. Houston, TX: Society of Exploration Geophysicists, pp. 4623–4627.
- Peng, C. & Meng, J. (2016) Inversion-based 3D deblending of towed-streamer simultaneous source data using sparse tau-p and wavelet transforms. In *86th SEG Annual International Meeting, Expanded Abstracts*. Houston, TX: Society of Exploration Geophysicists, pp. 4607–4611.
- Sen, S., Liu, Z., Sheng, J. & Wang, B. (2014) Reweighted thresholding and orthogonal projections for simultaneous source separation. In *84th SEG Annual International Meeting, Expanded Abstracts*. Houston, TX: Society of Exploration Geophysicists, pp. 243–248.
- Spitz, S., Hampson, G. & Pica, A. (2008) Simultaneous source separation: a prediction-subtraction approach. In *78th SEG Annual International Meeting, Expanded Abstracts*. Houston, TX: Society of Exploration Geophysicists, pp. 2811–2815.
- Spratt, S. (1988) Adaptive processing using Gabor transformation. In *58th SEG Annual International Meeting, Expanded Abstracts*. Houston, TX: Society of Exploration Geophysicists, pp. 1255–1257.
- Sun, J., Hou, S., Vinje, V., Poole, G. & Gelius, L.J. (2022) Deep learning-based shot-domain seismic deblending. *Geophysics*, 87, V215–V226.
- Sun, J., Slang, S., Elboth, T., Larsen Greiner, T., McDonald, S. & Gelius, L.J. (2020) A convolutional neural network approach to deblending seismic data. *Geophysics*, 85, WA13–WA26.

- Tang, Y. & Biondi, B. (2009) Least-squares migration/inversion of blended data. In *79th SEG Annual International Meeting, Expanded Abstracts*. Houston, TX: Society of Exploration Geophysicists, pp. 2859–2863.
- Trad, D., Siliqi, R., Poole, G. & Boelle, J.L. (2012) Fast and robust deblending using apex shifted radon transform. In *82nd SEG Annual International Meeting, Expanded Abstracts*. Houston, TX: Society of Exploration Geophysicists, pp. 1–5.
- van den Berg, E. & Friedlander, M.P. (2007) SPGL1: a solver for large-scale sparse reconstruction. <https://friedlander.io/spgl1>
- van den Berg, E. & Friedlander, M.P. (2008) Probing the Pareto frontier for basis pursuit solutions. *SIAM Journal on Scientific Computing*, 31, 890–912.
- Wang, B., Li, J. & Han, D. (2022) Iterative deblending using MultiResUNet with multilevel blending noise for training and transfer learning. *Geophysics*, 87, V205–V214.
- Wang, K. & Hu, T. (2022) Deblending of seismic data based on neural network trained in the CSG. *IEEE Transactions on Geoscience and Remote Sensing*, 60, 1–12.
- Wang, K., Hu, T. & Wang, S. (2022) An unsupervised learning approach to deblend seismic data from denser shot coverage surveys. *Geophysical Journal International*, 231, 801–816.
- Wang, K., Mao, W., Song, H. & Evinemi, E.I. (2022) A multi-data training method for a deep neural network to improve the separation effect of simultaneous-source data. *Geophysical Prospecting*, 71, 63–84.
- Wason, H., Herrmann, F.J. & Lin, T. T.Y. (2011) Sparsity-promoting recovery from simultaneous data: a compressive sensing approach. In *81st SEG Annual International Meeting, Expanded Abstracts*. Houston, TX: Society of Exploration Geophysicists, pp. 6–10.
- Wason, H., Kumar, R., Herrmann, F.J. & Aravkin, A.Y. (2014) Source separation via SVD-free rank minimization in the hierarchical semi-separable representation. In *SEG Technical Program Expanded Abstracts 2014*. Houston, TX: Society of Exploration Geophysicists, pp. 120–126.
- Wu, S., Blacqui re, G. & van Groenestijn, G.J. (2015) Shot repetition: an alternative approach to blending in marine seismic. In *85th SEG Annual International Meeting, Expanded Abstracts*. Houston, TX: Society of Exploration Geophysicists, pp. 120–126.
- Wu, S., Groenestijn, G.J.V. & Blacqui re, G. (2016) Using the source ghost in blended marine acquisition. In *86th SEG Annual International Meeting, Expanded Abstracts*. Houston, TX: Society of Exploration Geophysicists, pp. 87–91.
- Yu, Z., Abma, R., Etgen, J. & Sullivan, C. (2017) Attenuation of noise and simultaneous source interference using wavelet denoising. *Geophysics*, 82, V179–V190.
- Zhan, C., Malik, R., Specht, J., Liu, Z. & Teixeira, D. (2015) Deblending of continuously recorded OBN data by subtraction integrated with a median filter. In *85th SEG Annual International Meeting, Expanded Abstracts*. Houston, TX: Society of Exploration Geophysicists, pp. 4673–4677.
- Zhang, Y., Zhang, M., Wei Zhou, H. & Zou, Z. (2013) Separation of ISS seismic data via vector median filter in T-X and F-X domains. In *83rd SEG Annual International Meeting, Expanded Abstracts*. Houston, TX: Society of Exploration Geophysicists, pp. 4377–4381.
- Zhou, Y., Chen, W., Gao, J. & Pascal, F. (2013) Seismic deblending by sparse inversion over dictionary learning. In *83rd SEG Annual International Meeting, Expanded Abstracts*. Houston, TX: Society of Exploration Geophysicists, pp. 273–278.
- Zu, S., Cao, J., Qu, S. & Chen, Y. (2020) Iterative deblending for simultaneous source data using the deep neural network. *Geophysics*, 85, V131–V141.
- Zu, S., Zhou, H., Chen, Y., Chen, H., Cao, M. & Xie, C. (2016) A marine field trial for iterative deblending of simultaneous sources. In *86th SEG Annual International Meeting, Expanded Abstracts*. Houston, TX: Society of Exploration Geophysicists, pp. 113–118.
- Zu, S., Zhou, H., Li, Q., Chen, H., Zhang, Q., Mao, W. & Chen, Y. (2017) Shot-domain deblending using least-squares inversion. *Geophysics*, 82, V241–V256.
- Zu, S., Zhou, H., Mao, W., Gong, F. & Huang, W. (2018) 3d deblending of simultaneous source data based on 3D multi-scale shaping operator. *Journal of Applied Geophysics*, 151, 274–289.

How to cite this article: Kontakis, A. & Verschuur, D.J. (2023) Focal deblending: Marine data processing experiences. *Geophysical Prospecting*, 1–20. <https://doi.org/10.1111/1365-2478.13404>